Efficient switching of mCherry fluorescence using chemical caging

Bas M. C. Cloin[a,1], Elke De Zitter[b,1], Desiree Salas[a], Vincent Gielen[b], Gert E. Folkers[c], Marina Mikhaylova[a], Maike Bergeler[d], Bartosz Krajnik[e,f], Jeremy Harvey[d], Casper C. Hoogenraad[a], Luc Van Meervelt[b], Peter Dedecker[b,2], and Lukas C. Kapitein[a,2]

[a]Cell Biology, Department of Biology, Faculty of Science, Utrecht University, 3584 CH Utrecht, The Netherlands; [b]Biochemistry, Molecular and Structural Biology, Department of Chemistry, KU Leuven, 3001 Heverlee, Belgium; [c]NMR Spectroscopy, Department of Chemistry, Faculty of Science, Utrecht University, 3584 CH Utrecht, The Netherlands; [d]Quantum Chemistry and Physical Chemistry, Department of Chemistry, KU Leuven, 3001 Heverlee, Belgium; [e]Molecular Imaging and Photonics, Department of Chemistry, KU Leuven, 3001 Heverlee, Belgium; and [f]Institute of Physics, Faculty of Physics, Astronomy, and Informatics, Nicolaus Copernicus University, 87-100 Torun, Poland

Edited by Steven G. Boxer, Stanford University, Stanford, CA, and approved May 18, 2017 (received for review October 20, 2016)

Fluorophores with dynamic or controllable fluorescence emission have become essential tools for advanced imaging, such as superresolution imaging. These applications have driven the continuing development of photoactivatable or photoconvertible labels, including genetically encoded fluorescent proteins. These new probes work well but require the introduction of new labels that may interfere with the proper functioning of existing constructs and therefore require extensive functional characterization. In this work we show that the widely used red fluorescent protein mCherry can be brought to a purely chemically induced blue-fluorescent state by incubation with β-mercaptoethanol (βME). The molecules can be recovered to the red fluorescent state by washing out the βME or through irradiation with violet light, with up to 80% total recovery. We show that this can be used to perform single-molecule localization microscopy (SMLM) on cells expressing mCherry, which renders this approach applicable to a very wide range of existing constructs. We performed a detailed investigation of the mechanism underlying these dynamics, using X-ray crystallography, NMR spectroscopy, and ab initio quantum-mechanical calculations. We find that the βME-induced fluorescence quenching of mCherry occurs both via the direct addition of βME to the chromophore and through βME-mediated reduction of the chromophore. These results not only offer a strategy to expand SMLM imaging to a broad range of available biological models, but also present unique insights into the chemistry and functioning of a highly important class of fluorophores.

fluorescent proteins | mCherry | localization microscopy | β-mercaptoethanol | photoactivation

Fluorescent proteins have greatly advanced the study of intracellular organization and dynamics (1–3). For example, the discovery of red fluorescent proteins (RFPs) has enabled multicolor imaging when combined with the original green fluorescent protein (GFP), whereas the development of photoconvertible proteins whose fluorescence emission can be either activated or altered has enabled studying protein dynamics and turnover, as well as diffraction-unlimited imaging through a range of different approaches (1, 3–5). Single-molecule localization microscopy [SMLM (6)], for example, depends on the semicontrolled switching of fluorophores between dark states and fluorescent states, which facilitates repetitive sparse sampling and nanometric localization of individual fluorophores. In contrast to synthetic fluorophores, where blinking is often induced by transient interactions between the dye and buffer components such as reducing agents (7), blinking in FPs is typically achieved through the use of photoactivatable variants whose emission spectrum changes upon exposure to specific wavelengths, which is largely independent of buffer conditions. This change can be irreversible, such as fluorescence activation (8, 9) or green to red photoconversion (10–12), or reversible on/off switching (13, 14). For example, photoactivatable GFP (PA-GFP) switches from dark to green fluorescent upon exposure to violet light, whereas mEos switches from green to red fluorescence in the same conditions (3).

The wide applicability of these types of "smart labels" has sparked a broad interest in development of new probes and in understanding the underlying structural mechanisms. In the case of fluorescent proteins, these fluorescence dynamics typically result from decarboxylation of a glutamate residue in the protein environment, extension of the conjugated system of the chromophore with a histidine residue, or *cis*/*trans* isomerization of the chromophore coupled to a change in protonation state (15). However, despite intensive efforts, rational fluorescent protein design has remained difficult due to the high structural complexity of these probes, the complex and subtle relation between the structural and spectroscopic properties, and the fact that these processes are difficult to synchronize at the ensemble level.

The downside to using engineered photoactivatible labels is that these require the construction and introduction of new labeling constructs, which can be costly and laborious. Introducing different types of FPs can also lead to perturbations of the

Significance

In contrast to diffraction-limited microscopy, superresolution microscopy highly depends on the used fluorescent label. However, introducing a new label with suitable dynamics is not always straightforward. Here we describe how mCherry, a frequently used fluorescent protein in conventional microscopy, can be used for superresolution microscopy via a new caging mechanism involving the addition of β-mercaptoethanol. Moreover, we investigate the structural mechanism behind this chemical caging, using X-ray crystallography, NMR spectroscopy, and ab initio quantum mechanical calculations. These show that the mechanism is twofold: β-mercaptoethanol adds covalently to the protein's chromophore, whereas it also acts as a reducing agent for the chromophore.

Author contributions: B.M.C.C., E.D.Z., J.H., C.C.H., L.V.M., P.D., and L.C.K. designed research; B.M.C.C., E.D.Z., D.S., V.G., G.E.F., M.M., M.B., and B.K. performed research; M.M. contributed new reagents/analytic tools; B.M.C.C., E.D.Z., D.S., V.G., G.E.F., P.D., and L.C.K. analyzed data; B.M.C.C., E.D.Z., M.B., B.K., J.H., L.V.M., P.D., and L.C.K. wrote the paper; and P.D. and L.C.K. supervised the project.

The authors declare no conflict of interest.

This article is a PNAS Direct Submission.

Freely available online through the PNAS open access option.

Data deposition: The atomic coordinates and structure factors have been deposited in the Protein Data Bank, www.pdb.org (PDB ID code 5FHV).

[1]B.M.C.C. and E.D.Z. contributed equally to this work.

[2]To whom correspondence may be addressed. Email: l.kapitein@uu.nl or peter.dedecker@chem.kuleuven.be.

This article contains supporting information online at www.pnas.org/lookup/suppl/doi:10.1073/pnas.1617280114/-/DCSupplemental.

cellular biology, requiring extensive validation efforts. Finally, for many photoactivatable FPs the activation efficiency is only around 50% (16), leaving half of the fluorophores undetected. For this reason, several investigators have explored the use of conventional FPs, such as GFP and YFP, for subdiffraction imaging, because they will blink either spontaneously or in specific conditions (17, 18). Recently, also SMLM with a conventional red FP has been achieved by exploiting a light-induced dark state of mCherry in the presence of the reducing agent β-mercaptoethylamine (19). Unfortunately, using a light-induced dark state can lead to premature photodestruction of the fluorophores before the start of the single-molecule image acquisition, resulting in suboptimal SMLM images.

Here we show that mCherry can be brought to a purely chemically induced dark state from which up to 80% of the fluorophores can be recovered to the fluorescent state. Incubating with β-mercaptoethanol (βME) quenches the fluorescence peak at 610 nm and introduces a fluorescence peak at 460 nm, which can be reversed by illumination with violet light or by βME washout. We find that this chemical caging can be used for mCherry-based SMLM, which should be widely applicable, given the many existing mCherry fusion proteins. Spectroscopic characterization provided insights into the kinetics of this process, whereas X-ray crystallography, NMR spectroscopy, and ab initio calculations demonstrate a unique mechanism in which βME can convert mCherry to a blue fluorescent protein both by reducing the chromophore and by covalent addition to the C_β of the chromophore's tyrosine. This discovery brings insights into the chemistry and functioning of a highly important class of fluorophores.

Results and Discussion

The effect of βME on RFPs was first observed in fixed COS-7 cells expressing mCherry-tubulin. The bright red fluorescence in these cells was largely quenched after addition of 286 mM (2% vol/vol) βME (Fig. 1*A*), but could be recovered with violet light from a mercury lamp. After optimization, we could recover 73% ± 4% (average ± SEM) of the initial red fluorescence (Fig. 1*B*), demonstrating that mCherry-tubulin can be chemically caged by βME and subsequently photoactivated to recover the red fluorescent state. To examine how uncaging efficiency depends on the intensity of activation light, purified mCherry was nonspecifically adsorbed onto glass coverslips, quenched by incubation with 286 mM βME in PBS, and subsequently activated by different exposure periods (0–15 s) at different intensities of 405 nm laser light (Fig. 1*C*). At the lowest intensity, we observed that uncaging first increased and then saturated with increasing exposure time. At higher intensities, longer exposures resulted in less fluorescence and also the maximum achievable fluorescence intensity was lower at increasing activation intensities.

The data were fitted with a model describing a photoinduced transition from a caged to a fluorescent state and photodamaging pathways from both the caged state and the fluorescent state, with rates k_{pa}, $k_{dam,B}$, and $k_{dam,R}$, respectively (Fig. 1*D*). As expected, the photoactivation rate and the photodamage rates increased with increasing 405-nm laser intensity (Fig. 1*E*). The linear fit of $k_{dam,B}$ approximately went through the origin, implying no photodamage without 405 nm light. In contrast, the fit of $k_{dam,R}$ had an offset, which can be explained by recaging of photoactivated molecules. The photoactivation rate also increased with laser intensity, but to a lesser extent at higher laser powers. Together, these results explain why the amount of molecules returning to the fluorescent state is highest when low photoactivation intensities are used. Using these activation settings, we found that mCherry, mRFP, and tagRFP were caged by βME to 7.1% ± 0.4%, 1.3% ± 0.5%, and 50.5% ± 0.2% of the original intensity, respectively, whereas the return percentages using violet illumination were 77% ± 2%, 10.4% ± 2.8%, and 103% ± 3% (mean ± SEM, Fig. 1*F*).

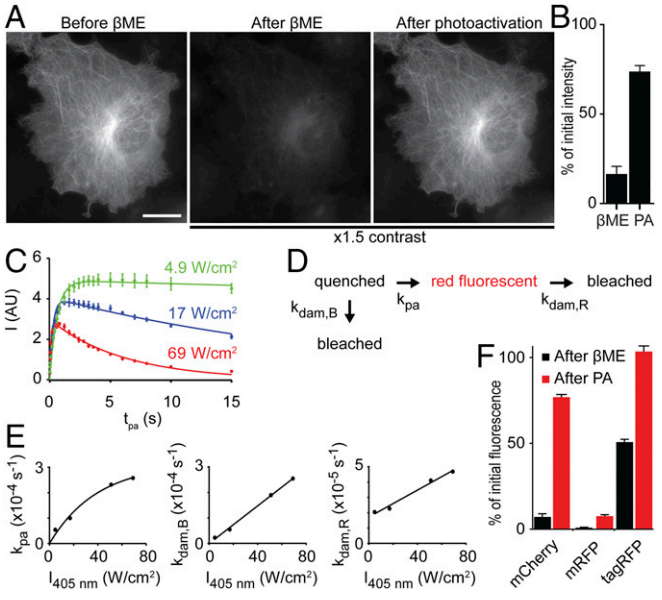

Fig. 1. RFPs can be caged by βME and uncaged by violet light. (*A*) Widefield images of a fixed COS-7 cell transfected with mCherry-tubulin, showing the initial fluorescence signal (*Left*), the fluorescence signal after adding 286 mM βME (*Center*), and the fluorescence signal after photoactivation with violet light (*Right*). The image contrast in *Center* and *Right* is 1.5 times that in *Left*. (Scale bar, 20 μm.) (*B*) Quantification of the fluorescence signal of widefield images of COS-7 cells transfected with mCherry-tubulin after adding βME and after photoactivation as percentage of the initial fluorescence. The fluorescence signal after photoactivation is 73% ± 4% of the initial signal (average ± SEM of 10 cells). (*C*) Fluorescence intensity of purified mCherry molecules in the presence of 286 mM βME after photoactivation, as a function of photoactivation exposure times for three 405-nm laser intensities. Solid lines indicate fits with a model incorporating both photoactivation and photodamage. (*SI Methods*, $n = 6$ measurements per time point). (*D*) Schematic of the model used for fitting data in *E*. (*E*) Rates of photoactivation and photodamage as function of 405-nm laser intensity, obtained from the fits described in *C*. Solid lines represent exponential (k_{pa}) or linear ($k_{dam,R}$ and $k_{dam,B}$) fits. (*F*) Quantification of the fluorescence signal of purified mCherry, mRFP, and TagRFP molecules from TIRF imaging. Black and red bars indicate the percentage of initial fluorescence after adding 286 mM βME and after photoactivation with low 405-nm laser intensity, respectively. $n = 4$, 2, and 2 samples and $n = 40$, 24, and 20 measurements for mCherry, mRFP, and tagRFP, respectively.

We next tested whether the observed photoactivation of chemically caged mCherry could be used for SMLM. Indeed, mCherry-based localization microscopy of fixed cells expressing mCherry-tubulin in a buffer containing 143 mM βME resulted in an improved resolution with a high density of emitters contributing to the superresolution reconstruction. mCherry molecules could either be photoactivated in the presence of βME (Fig. 2*A*) or return spontaneously after washout of βME during acquisition of the first thousands of frames (Fig. 2*B*). In both cases, the average localization accuracy was 11 nm. Other mCherry-labeled structures could also be better resolved using this approach, for example highlighting the centriole using mCherry-CEP135, clathrin-coated pits and lattices (20) using mCherry-Clathrin Light Chain (21), and cortical microtubule stabilization complexes using mCherry-KANK1 (22) (Fig. 2 *C* and *D*). Thus, βME-based caging combined with either 405-nm reactivation or βME washout enables mCherry-based localization microscopy.

Interestingly, the photon counts per mCherry blinking event obtained after washout of βME were 54% higher than those obtained using photoactivation in the presence of βME (Fig. 2*F*). This could be caused by photodamage induced by the activation laser (Fig. 1 *C*–*E*) or by rapid βME-induced recaging. The high emitter densities in our images could suggest that fluorophores

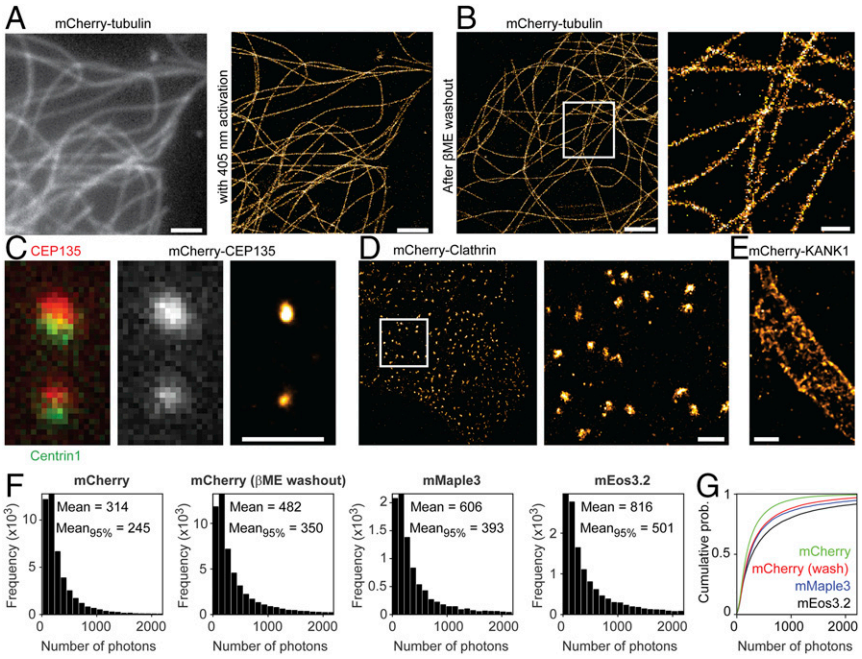

Fig. 2. Gradual uncaging enables superresolution imaging. (*A*) Widefield image of a COS-7 cell transfected with mCherry-tubulin (*Left*) and SMLM reconstruction of the same area (*Right*). SMLM was performed after addition of 143 mM βME. (Scale bars, 2 μm.) (*B*) SMLM reconstruction (*Left*) and zoom-in (*Right*) obtained by imaging after addition and washout of 286 mM βME, with no 405-nm activation during the first ~3,000 frames. [Scale bars, 2 μm (*Left*) and 500 nm (*Right*).] (*C*) (*Left* and *Center*) Zoom-in of HeLa cell coexpressing GFP-Centrin-1 (*Left*) and mCherry-CEP135 (*Center*). (*C*, *Right*) SMLM of the same area. SMLM was performed after addition of 143 mM βME. (Scale bar, 1 μm.) (*D* and *E*) SMLM reconstructions of HeLa cells expressing mCherry-Clathrin Light Chain1 (*D*, *Left*) and zoom-in (*D*, *Right*) or mCherry-KANK1 (*E*). SMLM was performed after addition of 143 mM βME. A median filter of pixel size 2 was applied. (Scale bars, 1 μm.) (*F*) Photon number measurements of mCherry, obtained in the presence of βME (*A*) or after βME washout (*B*), compared with mMaple3 and mEos3.2. All constructs were fused to tubulin. For calculating the indicated mean photon numbers, also counts outside the histogram (i.e., counts >2,200) were included. $Mean_{95\%}$ indicates the average photon count of the dimmest 95% blinking events for each type of sample. (*G*) Cumulative probability of photon counts for all four situations.

have multiple emission episodes. For example, we observed over 2,100 blinking events in the upper centriole in Fig. 2*C*, whereas the copy number of CEP135 per centriole has been estimated to be 300–500 (23). To compare the photon counts of mCherry with well-established photoconvertible fluorophores, we created tubulin constructs fused to mEos3.2 (24) or mMaple3 (25). Whereas the histograms of mCherry photon counts upon βME washout are very similar to the histograms of mEos3.2 and mMaple3, the average photon counts for mCherry are 40% and 20% lower, respectively. Closer inspection revealed that the higher average values of mEos3.2 and mMaple3 were caused by a small fraction of long-lived emission events. Excluding the brightest 5% of all emission events for all fluorophores resulted in photon counts of mCherry that were 70% and 89% of mEos3.2 and mMaple3, respectively. In addition, we found that the contrast ratio between the on-state and off-state fluorescence was also very similar for these fluorophores (43 ± 19, 45 ± 13, and 40 ± 15 for mCherry, mEos3.2, and mMaple3, respectively). Thus, for the vast majority of molecules, mCherry performs comparably to mMaple3 and slightly worse than mEos3.2.

During photoactivation of mCherry-tubulin expressing and βME-quenched cells, we noted a faint blue fluorescence. To investigate this further, we recorded the fluorescence emission spectrum of purified mCherry in the presence of increasing βME concentrations and found that addition of βME reduced the emission peak at 610 nm, whereas a peak at 460 nm appeared, indicating blue fluorescence (Fig. 3*A*). The intensity decrease at 610 nm upon addition of βME and as a function of the βME concentration followed the expected behavior for a reversible bimolecular reaction ($I = I_0/(1 + K_{eq}[\beta ME])$), yielding a K_{eq} of 0.10 mM^{-1} (Fig. 3*B*). In addition to the emission spectrum, the absorbance spectrum of mCherry was also strongly altered upon addition of 286 mM βME. The absorbance peak at 590 nm decreased over time and a peak at 410 nm appeared (Fig. 3 *C* and *D*), which could be reversed by photoactivation with a 405-nm laser. These results indicate that βME converts mCherry molecules from a red fluorescent state to a blue fluorescent photoconvertible state with absorption maximum at 410 nm and fluorescence emission maximum at 460 nm.

To characterize the spontaneous return of mCherry to the red fluorescent state without photoactivation, coverslips with nonspecifically adsorbed mCherry molecules were incubated with 286 mM βME in PBS for 20 min and then washed extensively with PBS to remove the βME. Upon βME washout, the red fluorescence of mCherry returned over the course of 1 h, with an average recovery of 83% ± 3% of the initial intensity and a single-exponential time constant of $7.0 \cdot 10^2$ s (Fig. 3 *E*–*G*). In addition, we tested whether other fluorescent proteins could be caged using βME. Remarkably, βME caging could be observed only for mCherry and some other red fluorescent proteins like mRFP1, TagRFP-T, and monomeric dsRed, but not for FPs with other colors or red FPs such as tdTomato and mKate2 (Table S1).

The βME-induced blue fluorescent state that we observed resembles the blue intermediate state reported in the maturation pathway of RFPs (26) and also matches the absorption and emission spectra reported for mTagBFP (27). Interestingly, exposure to violet light was found to accelerate the transition from the blue intermediate state to the final red state for dsRed (26), for mCherry-derived fluorescent timers, and for photoactivatable PAmCherry (9, 28). We therefore hypothesized that the addition of βME returns the RFP chromophore to a state similar to the blue intermediate state. The structure of the blue intermediate chromophore has been elucidated using X-ray crystallography (29) and ab initio quantum mechanics/molecular mechanics (QM/MM) calculations (30) and based on the reported differences in structure between the red fluorescent and blue fluorescent chromophore, we envisioned (at least) two ways for βME to interact with the chromophore to return it to the blue state (Fig. 4*A*). In the first mechanism, βME binds directly to the C_β of the tyrosine, whereas in the second mechanism βME causes a chemical reduction of the chromophore without covalent addition. In both cases the conjugated system would be interrupted at the C_β atom, resulting in the formation of an mTagBFP-type chromophore, with the shortening of the conjugated π system leading to the blue shift of the absorption and emission wavelengths.

To investigate the structural changes caused by βME, we crystallized mCherry and soaked it in a 2-M βME-containing solution just before flash freezing. Absorption measurements demonstrated that crystallized mCherry shows a similar blue shift in absorbance spectrum as noncrystallized mCherry and loses its red/purple color after soaking (Fig. S1 *A*–*C*). The crystal structure was determined with a resolution of 1.55 Å (Table S2) and

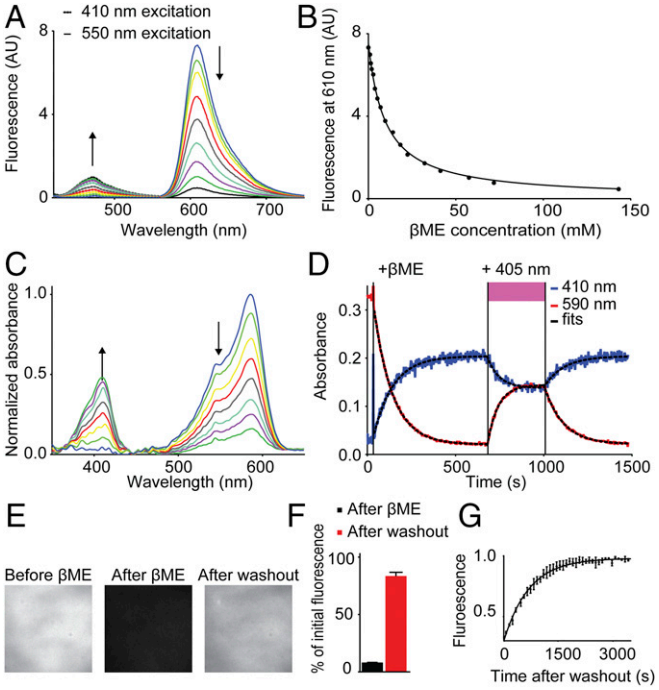

Fig. 3. βME transforms mCherry into a blue fluorescent protein. (*A*) Fluorescence spectra of in vitro mCherry molecules incubated with various βME concentrations, excited with 410 nm light (dotted lines) and 550 nm light (solid lines). Arrows indicate increasing βME concentration. (*B*) Quantification of mCherry fluorescence intensity at 610 nm as function of βME concentration. Solid line represents a fit of the fluorescence intensity according to an equation for a reversible bimolecular reaction $I = I_0 /(1 + K_{eq}\cdot[\beta ME])$, yielding K_{eq} = 0.10 mM^{-1} ($N = 1$, $n = 4$). (*C*) Absorbance spectra of in vitro mCherry molecules over time after addition of 286 mM βME. Arrows indicate increasing time. (*D*) Absorbance of purified mCherry molecules at 410 nm (black line) and 590 nm (red line) as a function of time. Addition of 286 mM βME and exposure to 405 nm light are indicated. Dotted black lines represent fits for one phase decay: $I = Plateau + (I_0 - Plateau)\cdot\exp(-t/\tau)$. Values for τ are 111 s^{-1} and 106 s^{-1} after βME, 65 s^{-1} and 60 s^{-1} during 405 nm illumination, and 109 s^{-1} and 108 s^{-1} after 405 nm illumination, for absorbance at 410 nm and 590 nm, respectively. (*E*) Fluorescence images of purified mCherry molecules on a coverslip before addition of 286 mM βME, after addition of βME, and 1.5 h after washout of βME. (*F*) Quantification of the fluorescence signal after addition of 286 mM βME (8% ± 0.1%) and 1.5 h after washout (83% ± 3%) (mean ± SEM; $N = 2$, $n = 44$ regions). (*G*) Kinetics of fluorescence return after βME washout. Fluorescence intensity is normalized to the final value. The solid line represents a fit for one phase dissociation of βME and mCherry, yielding $\tau = 7.0\cdot10^2$ s (95% confidence interval $6.6\cdot10^2$–$7.4\cdot10^2$; $N = 3$).

displayed the typical β-barrel structure seen in other fluorescent proteins. Whereas most amino acid residues were well defined in the electron density maps, the region around the chromophore in the center of the barrel was initially less clear. We were able to model two different chromophore types in this electron density: a chromophore closely resembling that of untreated mCherry (with occupancy of 59%), and a variant in which βME adds to the C_β of the tyrosine via its mercapto group (with occupancy of 41%) (Fig. 4 *B*–*D*). Although clear evidence for these two types was found, during structure refinement peaks in the $2F_o$–F_c electron density map suggest the existence of alternative conformations of the free βME tail (Fig. S1 *D* and *E*).

Whereas the crystal structure occupancies suggest that only about 41% of the mCherry molecules contain a βME adduct, the purple color of the crystal fully disappeared and the absorbance completely shifted to violet wavelengths upon addition of βME (Fig. S1 *A* and *B*). Although the partial occupancy could be caused by βME not having sufficient time before flash freezing, an image of the crystal on the goniometer head in the 100-K nitrogen stream just before X-ray data acquisition confirms that the crystal had fully lost its characteristic purple color (Fig. S1*C*). As a result, our data suggest that the remaining 59% does not correspond to the native mCherry chromophore, but rather to a chromophore in which the tyrosine C_β is in the reduced state, albeit with non-optimal bond angles for the C_β sp^3-hybridized carbon atom. Such deviations from model values are often observed in fluorescent protein chromophores. Further support for this model comes from our 2D [^{1}H,^{13}C] heteronuclear single quantum correlation (HSQC) measurements using ^{13}C/^{15}N tyrosine, methionine, and glycine-labeled mCherry (Fig. S2). Upon addition of βME, an extra peak emerged in the ^{13}C-^{1}H spectrum close to the characteristic C_β resonance for tyrosine. This suggests that the double bond between the C_α and C_β is converted to a single bond, resulting in blue-shifted absorption and emission. This peak most likely corresponds to the reduced state, because the covalent attachment of βME to the C_β that was observed in the crystal structure is expected to induce a nontraceable shift away from the characteristic tyrosine C_β resonance.

Despite the clear evidence for both reduction of and βME addition to the chromophore, the analyzed crystal structure did contain some peaks in the F_o–F_c difference electron density maps (Fig. S1*F*) that could not solely be explained by assuming conformational freedom for the free βME tail of the addition product. Moreover, we observed two conformations for lysine 70 and a lower occupancy of water molecule 436. Without these structural rearrangements, addition of βME would sterically not be possible, suggesting that the other possible enantiomer of the Michael addition cannot be accommodated by the β-barrel and cannot explain this residual electron density. Because we could not straightforwardly identify the missing structures or conformations, we next used quantum-chemical calculations on a model system of the chromophore (Fig. S3) to obtain detailed structures of possible βME-conjugated products (Fig. S4) and predict their absorption wavelengths (Table S3). These calculations were performed using coupled-cluster and time-dependent and time-independent density functional theory (*SI Computation of Electronic States* and Table S3).

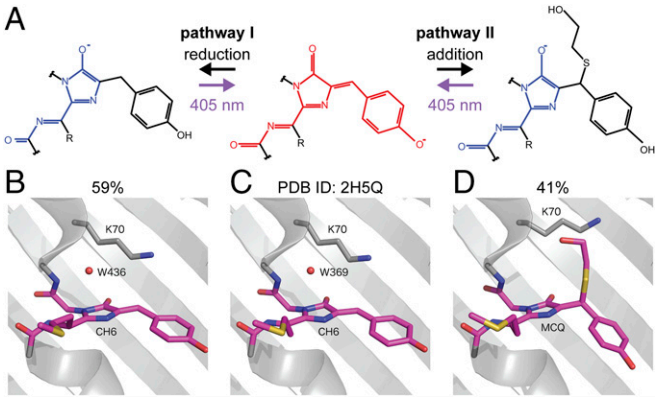

Fig. 4. mCherry caging occurs through Michael addition of βME to the chromophore. (*A*) Two hypothesized pathways for βME-induced conversion of the RFP chromophore from the red fluorescent form to the blue fluorescent form. Pathway I is via reduction of the double bond between the C_α and C_β of the tyrosine. In pathway II, βME is covalently attached to the C_β of the tyrosine through a Michael addition, removing the double bond between the C_α and C_β of the tyrosine. (*B*–*D*) Crystal structures of mCherry. *C* depicts the structure found in the PBD (ID: 2H5Q), whereas *B* and *D* depict the structures obtained after soaking a crystal in βME. The structure in *B* has 59% occupancy in the crystal vs. 41% occupancy in *D*.

The absorption wavelengths for the mCherry chromophore matched very well with the experimental observation (579 nm vs. 587 nm experimentally). Of all tested structures featuring addition of βME, only two showed an absorption wavelength consistent with the experimental observations (434 nm and 419 nm calculated vs. 410 nm experimentally). The structure with calculated absorption at 434 nm corresponds with the formation of a linear adduct on the C_β carbon atom of the chromophore's tyrosine, whereas the other structure (419 nm) involves the formation of a five-membered spiro ring structure by double addition of βME at the same position. The X-ray data do not provide conclusive evidence for or disprove the presence of this structure. However, we consider it unlikely that this structure is formed because it would require an addition–oxidation–addition mechanism and the formation of acetals from βME is known to occur only under harsh conditions (31). Therefore, we propose that, of these structures, only the linear adduct (Fig. 5*D*) is formed. Of the structures that involve a reduction of the chromophore, both the structure initially suggested based on the NMR experiments (Fig. 5*B*) and an additional one involving reduction elsewhere in the chromophore lead to predicted absorption wavelengths consistent with experiment (411 nm and 443 nm, respectively). Our NMR data directly support the formation of the structure in Fig. 5*B*, but we do not have any direct data that prove or disprove the formation of the other reduced structure shown in Fig. 5. However, in our view the direct experimental support for the structures in Fig. 5 *B* and *D* and the high similarity of the absorption spectra to mTagBFP indicate that the structures proposed in Fig. 4 are most likely the chemical species formed in this process.

In summary, we have shown that mCherry can be chemically brought to a blue fluorescent state by βME and returned to the red fluorescent state by photoactivation with violet light or by βME washout. The crystallographic data unambiguously showed the appearance of electron density that can be explained only by the formation of a covalent bond at the C_β atom of tyrosine 67, resulting in a blue fluorescent chromophore. Covalent addition of thiols has been previously reported for cyanine dyes (32), although in that case the addition required irradiation with light, whereas here quenching occurs in the absence of light. Other groups have observed a similar spontaneous addition of thiol compounds (33) and phosphine (34) to fluorophores, but to our knowledge this has not been previously shown for fluorescent proteins. We propose that the covalent modification of the chromophore occurs via a Michael addition through the SH group of βME. Reversibility of Michael additions has been shown for different addends and adducts (35, 36). For example, reversible Michael addition of a thiol to a fluorescent probe was shown to blue shift the absorbance and fluorescence spectra, allowing the measurement of glutathione concentration inside living cells (37).

We observed that βME can cage some, but not all RFPs. We believe that the ability and the magnitude of βME-induced caging depend on several factors, such as the allowance for βME to enter the β-barrel, the accessibility of the chromophore C_β atom, the possibility for the lysine-70 conformational change upon Michael addition, and the possibility to change the C_β hybridization following the Michael addition or reduction.

It is important to note that the additional covalent bond with βME was present in about 40% of mCherry molecules in the crystal, whereas the whole crystal changed color upon soaking in βME. This suggests that the quenching of the other 60% of the molecules is achieved by reduction of the tyrosine C_β atom, consistent with the appearance of the characteristic tyrosine C_β resonance in the NMR spectrum. Remarkably, irradiation with violet light could reverse both the reduction and the addition, given that the maximum recovery is about 80%. These mechanisms facilitate the use of conventional RFPs in SMLM. Here, the purely chemical transition to a dark state using βME decouples imaging laser power and duty ratio, which allows optimizing imaging conditions for single-molecule detection. This could be an advantage compared with using a light-induced dark state, as reported for mCherry in the presence of β-mercaptoethylamine (19). Given the many existing mCherry-based model systems, our strategy for mCherry-based SMLM using chemical caging followed by highly efficient photoactivation should be widely applicable.

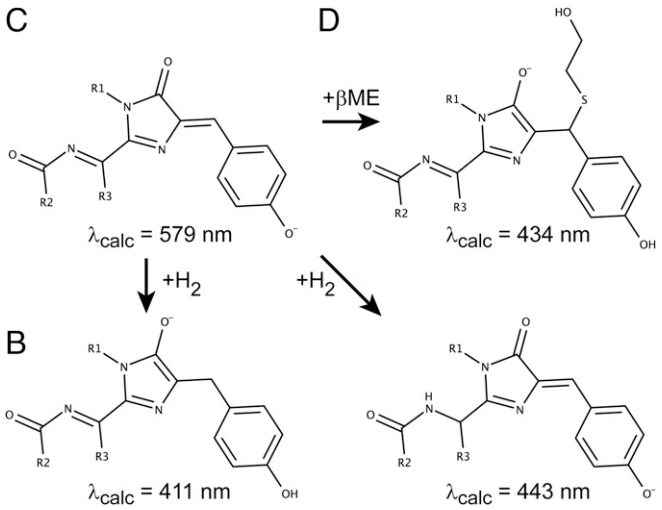

Fig. 5. Quantum chemical calculations predict three possible reaction products. Three possible chromophore types can theoretically be formed after addition of βME, based on their RICC2/Def2TZVP absorption wavelength (indicated below each structure in nanometers). Structure names *B*, *C*, and *D* refer to the crystal structures shown in Fig. 4 *B*–*D* (reduced state, unreacted state, and linear adduct, respectively).

Materials and Methods

Microscopy. All microscopy was performed on a Nikon Ti-E microscope equipped with a 100× Apo TIRF (N.A. 1.49) objective and a Perfect Focus System. Excitation was done either with a mercury lamp or via a custom illumination pathway with a 15-mW 405-nm diode laser (Power Technology) and a 100-mW 561-nm DPSS laser (Cobolt Jive). Fluorescence was detected using either an Andor DU-897D EMCDD with an additional 2.5× Optovar to achieve an effective pixel size of 64 nm or an Andor NEO 5.5 sCMOS with an effective pixel size of 65 nm. All components were controlled by Micromanager software (38). For intensity measurements as a function of photoactivation time an additional diffuser (Optotune LSR-C-3010) was inserted between a pair of lenses with focal distance of 75 mm in the illumination pathway for even illumination in TIRF mode. For SMLM, samples were continuously illuminated with 561 nm light in combination with increasing 405 nm intensity to maintain a constant number of molecules in the fluorescent state. Typically 5,000–15,000 frames were recorded with exposure times of 40–60 ms.

Crystallography. mCherry crystals were grown in sitting drops containing 1 μL of protein solution (10 mg/mL), 1 μL of precipitant (0.2 M $MgCl_2 0.6H_2O$, 0.1 M Tris, pH 8.5, 25% PEG 4000), and 0.5 μL of βME (2 M), equilibrated against a 100-μL reservoir of precipitant. As the solution regained its color after several days, the crystals were soaked in a drop containing 1 μL PEG 400 (40%) and 1 μL βME (5 M) just before flash freezing in liquid nitrogen. Upon soaking, the crystals immediately lost their color and this absence of color remained until X-ray diffraction.

Data collection and refinement statistics can be found in Table S2. The structure was deposited in the PDB with accession code 5FHV. Images were created using the PyMOL Molecular Graphics System (Version 1.8; Schrödinger, LLC).

More experimental details and detailed information on the crystal structure determination and quantum-chemical calculations can be found in *SI Methods*.

ACKNOWLEDGMENTS. We are grateful to Roger Tsien, Xioawei Zhuang, Klemens Rottner, and Anna Akhmanova for sharing constructs; to Kai Jiang, Roderick Tas, and Max Adrian for cloning constructs; and to Anne

Janssen and York Ammon for technical assistance. We thank Wim Dehaen, Department of Chemistry, KU Leuven, for insightful discussion. This research was supported by the Dutch Technology Foundation (STW), which is part of the Netherlands Organisation for Scientific Research (NWO) Grant NWO-NANO 11421. Additional support came from the NWO Grant NWO-ALW-VIDI (to L.C.K.) and the European Research Council (ERC) Starting Grant 336291 (to L.C.K.). We also acknowledge support from the Research-Foundation Flanders (FWO) via Grants 1521915N, 1502314N, and 1525113N. M.M. is the recipient of a European Molecular Biology Organization (EMBO) Long-Term Fellowship (EMBO ALTF 88x4-2011), a Marie Curie IEF (FP7-PEOPLE-2011-IEF), and a DFG Emmy-Noether Grant Ml 1923/1-1. P.D. acknowledges support by the European Research Council via ERC Starting Grant 714688. E.D.Z. and V.G. thank the FWO Flanders for strategic basic research grants. B.K. received financial support from the Mobility Plus programme (1068/MOB/2013/0) founded by the Polish Ministry of Science and Higher Education. E.D.Z. and L.V.M. thank the staff of the beamline X60DA at the Swiss Light Source (Villigen, Switzerland) for their assistance with the data collection. M.B. gratefully acknowledges support from a fellowship from the Swiss National Science Foundation.

1. Miyawaki A (2011) Proteins on the move: Insights gained from fluorescent protein technologies. *Nat Rev Mol Cell Biol* 12:656–668.
2. Shaner NC, Patterson GH, Davidson MW (2007) Advances in fluorescent protein technology. *J Cell Sci* 120:4247–4260.
3. Shcherbakova DM, Sengupta P, Lippincott-Schwartz J, Verkhusha VV (2014) Photocontrollable fluorescent proteins for superresolution imaging. *Annu Rev Biophys* 43: 303–329.
4. Adam V, Berardozzi R, Byrdin M, Bourgeois D (2014) Phototransformable fluorescent proteins: Future challenges. *Curr Opin Chem Biol* 20:92–102.
5. Dedecker P, De Schryver FC, Hofkens J (2013) Fluorescent proteins: Shine on, you crazy diamond. *J Am Chem Soc* 135:2387–2402.
6. Patterson G, Davidson M, Manley S, Lippincott-Schwartz J (2010) Superresolution imaging using single-molecule localization. *Annu Rev Phys Chem* 61:345–367.
7. van de Linde S, Sauer M (2014) How to switch a fluorophore: From undesired blinking to controlled photoswitching. *Chem Soc Rev* 43:1076–1087.
8. Patterson GH, Lippincott-Schwartz J (2002) A photoactivatable GFP for selective photolabeling of proteins and cells. *Science* 297:1873–1877.
9. Subach FV, et al. (2009) Photoactivatable mCherry for high-resolution two-color fluorescence microscopy. *Nat Methods* 6:153–159.
10. Ando R, Hama H, Yamamoto-Hino M, Mizuno H, Miyawaki A (2002) An optical marker based on the UV-induced green-to-red photoconversion of a fluorescent protein. *Proc Natl Acad Sci USA* 99:12651–12656.
11. McEvoy AL, et al. (2012) mMaple: A photoconvertible fluorescent protein for use in multiple imaging modalities. *PLoS One* 7:e51314.
12. Wiedenmann J, et al. (2004) EosFP, a fluorescent marker protein with UV-inducible green-to-red fluorescence conversion. *Proc Natl Acad Sci USA* 101:15905–15910.
13. Ando R, Mizuno H, Miyawaki A (2004) Regulated fast nucleocytoplasmic shuttling observed by reversible protein highlighting. *Science* 306:1370–1373.
14. Duwé S, et al. (2015) Expression-enhanced fluorescent proteins based on enhanced green fluorescent protein for super-resolution microscopy. *ACS Nano* 9:9528–9541.
15. Shcherbakova DM, Verkhusha VV (2014) Chromophore chemistry of fluorescent proteins controlled by light. *Curr Opin Chem Biol* 20:60–68.
16. Durisic N, Laparra-Cuervo L, Sandoval-Álvarez A, Borbely JS, Lakadamyali M (2014) Single-molecule evaluation of fluorescent protein photoactivation efficiency using an in vivo nanotemplate. *Nat Methods* 11:156–162.
17. Fölling J, et al. (2008) Fluorescence nanoscopy by ground-state depletion and single-molecule return. *Nat Methods* 5:943–945.
18. Biteen JS, et al. (2008) Super-resolution imaging in live Caulobacter crescentus cells using photoswitchable EYFP. *Nat Methods* 5:947–949.
19. Winterflood CM, Ewers H (2014) Single-molecule localization microscopy using mCherry. *ChemPhysChem* 15:3447–3451.
20. Grove J, et al. (2014) Flat clathrin lattices: stable features of the plasma membrane. *Mol Biol Cell* 25:3581–3594.
21. Benesch S, et al. (2005) N-WASP deficiency impairs EGF internalization and actin assembly at clathrin-coated pits. *J Cell Sci* 118:3103–3115.
22. Bouchet BP, et al. (2016) Talin-KANK1 interaction controls the recruitment of cortical microtubule stabilizing complexes to focal adhesions. *eLife* 5:e18124.
23. Bauer M, Cubizolles F, Schmidt A, Nigg EA (2016) Quantitative analysis of human centrosome architecture by targeted proteomics and fluorescence imaging. *EMBO J* 35:2152–2166.
24. Zhang M, et al. (2012) Rational design of true monomeric and bright photoactivatable fluorescent proteins. *Nat Methods* 9:727–729.
25. Wang S, Moffitt JR, Dempsey GT, Xie XS, Zhuang X (2014) Characterization and development of photoactivatable fluorescent proteins for single-molecule-based superresolution imaging. *Proc Natl Acad Sci USA* 111:8452–8457.
26. Verkhusha VV, Chudakov DM, Gurskaya NG, Lukyanov S, Lukyanov KA (2004) Common pathway for the red chromophore formation in fluorescent proteins and chromoproteins. *Chem Biol* 11:845–854.
27. Subach OM, et al. (2008) Conversion of red fluorescent protein into a bright blue probe. *Chem Biol* 15:1116–1124.
28. Subach FV, et al. (2009) Photoactivation mechanism of PAmCherry based on crystal structures of the protein in the dark and fluorescent states. *Proc Natl Acad Sci USA* 106:21097–21102.
29. Subach OM, et al. (2010) Structural characterization of acylimine-containing blue and red chromophores in mTagBFP and TagRFP fluorescent proteins. *Chem Biol* 17: 333–341.
30. Bravaya KB, Subach OM, Korovina N, Verkhusha VV, Krylov AI (2012) Insight into the common mechanism of the chromophore formation in the red fluorescent proteins: The elusive blue intermediate revealed. *J Am Chem Soc* 134:2807–2814.
31. Djerassi C, Gorman M (1953) Studies in organic sulfur compounds. VI.1. Cyclic ethylene and trimethylene hemithioketals. *J Am Chem Soc* 75:3704–3708.
32. Dempsey GT, et al. (2009) Photoswitching mechanism of cyanine dyes. *J Am Chem Soc* 131:18192–18193.
33. Peng H, et al. (2012) Thiol reactive probes and chemosensors. *Sensors* 12: 15907–15946.
34. Vaughan JC, Dempsey GT, Sun E, Zhuang X (2013) Phosphine quenching of cyanine dyes as a versatile tool for fluorescence microscopy. *J Am Chem Soc* 135:1197–1200.
35. van Axel Castelli V, et al. (1999) Rates and equilibria of the Michael-type addition of benzenethiol to 2-cyclopenten-1-ones. *J Org Chem* 64:8122–8126.
36. Allen CFH, Happ GP (1964) The thermal reversibility of the Michael reaction: I. Nitriles. *Can J Chem* 42:641–649.
37. Chen J, Jiang X, Carroll SL, Huang J, Wang J (2015) Theoretical and experimental investigation of thermodynamics and kinetics of thiol-Michael addition reactions: A case study of reversible fluorescent probes for glutathione imaging in single cells. *Org Lett* 17:5978–5981.
38. Edelstein A, Amodaj N, Hoover K, Vale R, Stuurman N (2010) Computer control of microscopes using μManager. *Curr Protoc Mol Biol* 14:14.20.1–14.20.17.
39. Shaner NC, et al. (2004) Improved monomeric red, orange and yellow fluorescent proteins derived from Discosoma sp. red fluorescent protein. *Nat Biotechnol* 22: 1567–1572.
40. Bouchet BP, et al. (2016) Mesenchymal cell invasion requires cooperative regulation of persistent microtubule growth by SLAIN2 and CLASP1. *Dev Cell* 39:708–723.
41. Kapitein LC, et al. (2011) NMDA receptor activation suppresses microtubule growth and spine entry. *J Neurosci* 31:8194–8209.
42. Folkers GE, van Buuren BNM, Kaptein R (2004) Expression screening, protein purification and NMR analysis of human protein domains for structural genomics. *J Struct Funct Genomics* 5:119–131.
43. Goddard T, Kneller D (2008) *Sparky 3* (University of California, San Francisco).
44. Kabsch W (2010) XDS. *Acta Crystallogr D Biol Crystallogr* 66:125–132.
45. Evans PR, Murshudov GN (2013) How good are my data and what is the resolution? *Acta Crystallogr D Biol Crystallogr* 69:1204–1214.
46. McCoy AJ, et al. (2007) Phaser crystallographic software. *J Appl Cryst* 40:658–674.
47. Afonine PV, et al. (2012) Towards automated crystallographic structure refinement with phenix.refine. *Acta Crystallogr D Biol Crystallogr* 68:352–367.
48. Emsley P, Lohkamp B, Scott WG, Cowtan K (2010) Features and development of Coot. *Acta Crystallogr D Biol Crystallogr* 66:486–501.
49. Moriarty NW, Grosse-Kunstleve RW, Adams PD (2009) Electronic Ligand Builder and Optimization Workbench (eLBOW): A tool for ligand coordinate and restraint generation. *Acta Crystallogr D Biol Crystallogr* 65:1074–1080.
50. Lebedev AA, et al. (2012) JLigand: A graphical tool for the CCP4 template-restraint library. *Acta Crystallogr D Biol Crystallogr* 68:431–440.
51. Groom CR, Bruno IJ, Lightfoot MP, Ward SC (2016) The Cambridge Structural Database. *Acta Crystallogr B Struct Sci Cryst Eng Mater* 72:171–179.
52. Yanai T, Tew DP, Handy NC (2004) A new hybrid exchange–correlation functional using the Coulomb-attenuating method (CAM-B3LYP). *Chem Phys Lett* 393:51–57.
53. Grimme S, Antony J, Ehrlich S, Krieg H (2010) A consistent and accurate ab initio parametrization of density functional dispersion correction (DFT-D) for the 94 elements H-Pu. *J Chem Phys* 132:154104.
54. Ahlrichs R, Bar M, Haser M, Horn H, Kolmel C (1989) Electronic-structure calculations on workstation computers - the program system Turbomole. *Chem Phys Lett* 162: 165–169.
55. Schreiber M, Silva-Junior MR, Sauer SPA, Thiel W (2008) Benchmarks for electronically excited states: CASPT2, CC2, CCSD, and CC3. *J Chem Phys* 128:134110.
56. List NH, Olsen JM, Rocha-Rinza T, Christiansen O, Kongsted J (2012) Performance of popular XC-functionals for the description of excitation energies in GFP-like chromophore models. *Int J Quantum Chem* 112:789–800.
57. Topol I, Collins J, Savitsky A, Nemukhin A (2011) Computational strategy for tuning spectral properties of red fluorescent proteins. *Biophys Chem* 158:91–95.
58. Wanko M, García-Risueño P, Rubio A (2012) Excited states of the green fluorescent protein chromophore: Performance of ab initio and semi-empirical methods. *Physica Status Solidi B* 249:392–400.
59. Surdhar PS, Armstrong DA (1987) Reduction potentials and exchange reactions of thiyl radicals and disulfide anion radicals. *J Phys Chem* 91:6532–6537.